Imaging electron angular distributions to assess a full-power petawatt-class laser focus

Smrithan Ravichandran [1,2] Marine Huault [3,4] Roberto Lera [3] Calvin Z. He [1,2] Andrew Longman [5]
Robert Fedosejevs [6] Luis Roso [7] and Wendell T. Hill, III [1,2,8,*]

[1]*Institute for Physical Science and Technology, University of Maryland, College Park, Maryland 20742, USA*
[2]*Joint Quantum Institute, University of Maryland, College Park, Maryland 20742, USA*
[3]*Centro de Láseres Pulsados, 37185 Villamayor, Salamanca, Spain*
[4]*Departamento de Física Fundamental, Universidad de Salamanca, 37008 Salamanca, Spain*
[5]*Lawrence Livermore National Laboratory, Livermore, California 94550, USA*
[6]*Electrical and Computer Engineering, University of Alberta, Edmonton, Alberta T6G 2V4, Canada*
[7]*Departamento de Física Aplicada, Universidad de Salamanca, 37008 Salamanca, Spain*
[8]*Department of Physics, University of Maryland, College Park, Maryland 20742, USA*

We present a technique to assess the focal volume of petawatt-class lasers at full power. Our approach exploits quantitative measurement of the angular distribution of electrons born in the focus via ionization of rarefied gas, which are accelerated forward and ejected ponderomotively by the field. We show that a bivariate (θ, ϕ) angular distribution, which was obtained with image plates, not only enables the peak intensity to be extracted, but also reflects nonideality of the focal-spot intensity distribution. In our prototype demonstration at intensities of a few $\times 10^{19}$ to a few $\times 10^{20}$ W/cm^2, an f/10 optic produced a focal spot in the paraxial regime. This allows a plane-wave parametrization of the peak intensity given by $\tan \theta_c = 2/a_0$ (a_0 being the normalized vector potential and θ_c the minimum ejection angle) to be compared with our measurements. Qualitative agreement was found using an a_0 inferred from the pulse energy, pulse duration, and focal spot distribution with a modified parametrization, $\tan \theta_c = 2\eta/a_0$ ($\eta = 2.02^{+0.26}_{-0.22}$). This highlights the need for (i) better understanding of intensity degradation due to focal-spot distortions and (ii) more robust modeling of the ejection dynamics. Using single-shot detection of electrons, we showed that while there is significant shot-to-shot variation in the number of electrons ejected at a given angular position, the average distribution scales with the pulse energy in a way that is consistent with that seen with the image plates. Finally, we note that the asymptotic behavior as $\theta \to 0°$ limits the usability of angular measurement. For 800 nm, this limit is at an intensity $\sim 10^{21}$ W/cm^2.

I. INTRODUCTION

The recent proliferation of petawatt-class laser facilities [1] is driven by a two-pronged desire: creating extreme intensities in the laboratory [2,3] where new fundamental physics can be explored, and developing new laser-based technologies [4]. Pair production [5–8] and strong-field photon-photon scattering [9–12] are examples of the former. Secondary sources, particle accelerators and high-energy photon beams, are examples of the latter. While efforts are underway to upgrade or build bigger and more powerful lasers [13–18], instrumentation to characterize the focal spot, necessary to guide and improve designs, and to employ as experimental diagnostic tools, has not kept pace. Intensity estimates today, as it have been for some years, still largely rely on indirect approaches that either do not sample the full beam at full power or are not performed in real time. As such, these estimates tend to depend on extrapolations and assumed behavior of laser parameters that fail to account for real-time beam conditions and fluctuations, intensity-dependent degradation due

to spatiotemporal coupling [19], beam aberrations, and other nonlinear effects in the focus. Pulse-front tilts as small as 0.2 fs/mm due to slight imperfections in compressor gratings, for example, have been shown to reduce the intensity as much as an order of magnitude [20]. Clearly, new tools are needed.

Several approaches have been suggested to characterize the peak intensity at full power, exploiting concomitant processes with high intensities ($>10^{18}$ W/cm^2): radiation associated with relativistic Thomson scattering [21–24], appearance intensity of ionization stages of tenuous gases [25,26], and ponderomotive ejection of electrons [27–30]. For widespread use as a diagnostic, it is important that the method be straightforward to implement, minimally intrusive to the principal scientific study, sensitive to beam conditions and distortions, and capable of single-shot deployment. Thomson scattering in the 10^{18}–10^{19} W/cm^2 intensity range produces spectrally convenient Doppler-shifted, second harmonic radiation that is detectable with a gated spectrometer [24]. The spectrometer requirement, however, makes single-shot deployment challenging. At the same time, intensities $>10^{19}$ W/cm^2 cause harmonic orders to overlap, making them difficult to distinguish. While monitoring the fundamental is possible, midinfrared detection will be required. Ionization is

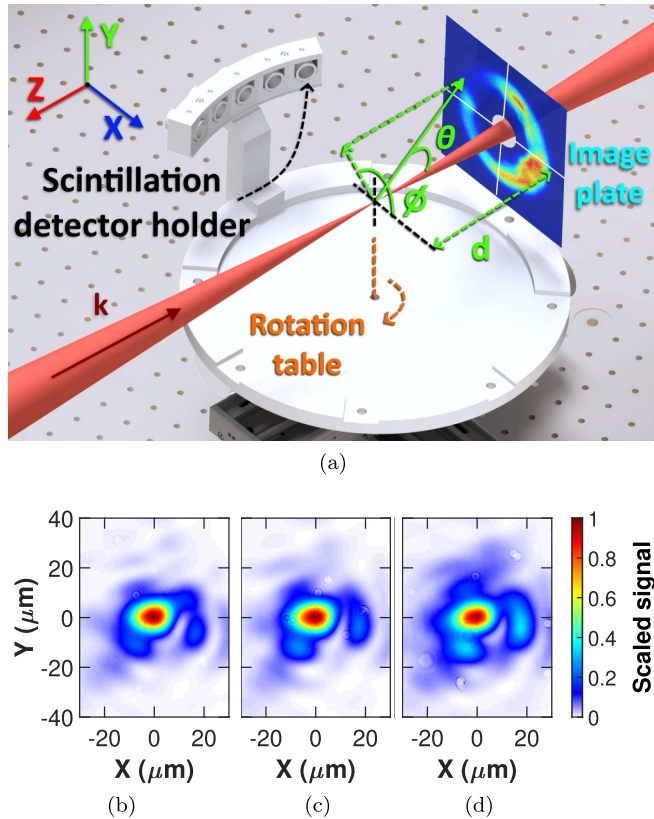*wth@umd.edu

(a)

(b)   (c)   (d)

FIG. 1. Experimental setup (not to scale) for image plate and scintillation detectors (a). Image plates are mounted a fixed distance, $d \approx 40$ mm, after the focus with active area facing the focal spot. Scintillation detectors (not shown) are mounted in the holder, attached to a rotation table, rotating about the focus in the $\vec{E}$-$\vec{k}$ (i.e., $\hat{x}$-$\hat{z}$) plane a fixed distance (≈ 138 mm) away. Typical VEGA-3 focal spot images obtained at low power are shown in (b)–(d).

single-shot capable but provides limited information on the intensity distribution in the focus. Moreover, ionization thresholds tend to be clumped together for certain intensities, with large gaps between thresholds at other intensities. This manuscript introduces a straightforward experimental technique upon which an *in situ* intensity-measurement tool might possibly be based. The approach exploits the angular distribution of electrons ejected from the focus. The electrons not only allow the intensity to be monitored, they reveal asymmetries in the intensity distribution within the focal volume.

Figure 1(a) shows the experimental schematic of nascent electrons being ejected into a bivariate (θ and ϕ) angular distribution (BiAD) that we measured using image plates. The BiAD measurements were taken under paraxial conditions that allowed us to test the validity of the plane-wave parametrization discussed below. Our measurements were done at pressures between 10^{-5} and 10^{-4} mbar. In this range, the image plates required ~ 100 laser shots. We also made single-shot measurements of the electrons with scintillation detectors.

This manuscript is organized as follows. We provide some background and outline the theory in Sec. II. In Sec. III, we describe the experiments. We present the results from our analysis of the BiADs in Sec. IV. We also compare the

measured $\tan \theta$ vs a_0 scaling with the theoretical predictions and discuss the limitations of this application for higher intensities. Finally, we present a road map for deployment as a tomographical tool and how it might be extended well beyond the current intensity record of 10^{23} W/cm^2 [2].

II. THEORY

It is well known that the ponderomotive force causes free electrons to experience an outward force from the focus of laser beams [31,32]. When the normalized vector potential, $a_0 = eE\lambda_0/2\pi m_e c^2 \approx 0.855\lambda_0(\mu\mathrm{m})\sqrt{I(\mathrm{W/cm^2})/10^{18}}$, exceeds 1, the laser accelerates electrons to relativistic energies within a single cycle. Here, e, E, λ_0, m_e, c, and I are the elementary charge, electric field magnitude, laser wavelength, electron mass, speed of light in vacuum, and peak laser intensity, respectively. Consequently, the magnetic and electric forces become comparable, resulting in the electrons gaining momentum along the direction of laser propagation. Due to the existence of longitudinal field components, as necessitated by Maxwell's equations, the electron ejection is not restricted to a plane [32]. Rather, electrons with a Lorentz factor γ are ejected into a cone about the wave vector $\vec{k}$ with apex angle $\theta(\gamma)$ that obeys [31,33]

$$\tan \theta = p_\perp/p_\parallel = \sqrt{2/(\gamma - 1)}, \tag{1}$$

where $p_\perp$ and $p_\parallel$ are the transverse and longitudinal components of the electron's momentum relative to $\vec{k}$, respectively. As electrons interact with higher laser intensities, γ increases, which decreases $p_\perp/p_\parallel$ and θ according to Eq. (1). Thus, one might expect the existence of a characteristic ejection cutoff angle θ_c for the BiAD of ejected electrons that reflects the peak intensity, or a_0, experienced by the electrons. The exact dependence of θ_c on a_0, however, requires knowledge of how the kinetic energy of the most energetic electrons with $\gamma = \gamma_p$ is related to a_0. While studies have considered this relationship in various contexts, how the ponderomotive force contributes to γ_p is not known analytically for a general case due to theoretical complications in treating the relativistic dynamics of the accelerated electrons. A plane-wave analysis by Hartemann *et al.* [31] predicts

$$\gamma_p = 1 + a_0^2/2 \tag{2}$$

for the interaction of free electrons with a linearly polarized field [28,29,34]. We note that for a focused laser pulse traveling along $-\hat{z}$ and polarized with E_x along $\hat{x}$ as shown in Fig. 1(a), the longitudinal component of the electric field E_z has a first-order contribution $\propto \partial E_x/\partial x$ [35–37]. For a TEM$_{00}$ Gaussian laser mode, it can be shown that the largest contribution scales as $E_z(r = w_0/\sqrt{2})/E_x(r = 0) \approx 1/(kw_0)$ [35], where r is the radial distance in the transverse plane and w_0 is the beam waist of the Gaussian laser beam. Therefore, as the f/# (f-number) of the focusing optic increases, E_z/E_x decreases. In our experiment, we used an off-axis f/10 parabolic mirror where $1/(kw_0) \approx 0.018$, which is in the paraxial limit.

We note there are other relationships between γ_p and a_0; $\gamma_p = \sqrt{1 + a_0^2/2}$ [38] is often considered in the context of energy absorption from a high-intensity laser pulse by an electron in a plasma [39,40]. It has also been considered for

TABLE I. Summary of experimental conditions used to measure θ_c with nitrogen gas. The U and τ (as defined in Sec. III B) reported here is the average value obtained over the corresponding sequence of shots, after considering the systematic uncertainties in the measurement process, which dominate the uncertainty in measuring the average. The techniques used to measure U and τ are detailed in Sec. III B. The sources for the uncertainty in θ_c are the error in positioning the image plate and in estimating where the signal cuts off as detailed in the text.

Fig.	Plate Type	No. of Shots	U (J) ($\pm 10\%$)	τ (fs) ($\pm 20\%$)	Pressure (mbar)	θ_c (deg)
2(a)	SR	100	23.0	35.4	4×10^{-5}	22 ± 1
2(b)	SR	100	23.4	55.4	7×10^{-5}	30 ± 1
2(c)	MS[a]	96	8.8	34.7	9×10^{-5}	39 ± 2

[a]MS plates were used for the lower-intensity measurement as they are more sensitive than the SR by a factor of $\sim$3.

free electrons in a laser field [26]. This scaling and that of Eq. (2) differ significantly in the value of a_0 for a given γ_p. For example, for $\gamma_p = 2$, a_0 according to Eq. (2) is 60% of that in $\gamma_p = \sqrt{1 + a_0^2/2}$. Thus, it is important to distinguish between conditions under which either is applicable, if at all, and test them to gain a better understanding of the role of the ponderomotive force in this relativistic intensity regime. While a direct quantitative measurement of a_0 may be complicated, we can test the plane-wave prediction of the dependence of θ_c as a function of a_0 by combining Eqs. (1) and (2) to give

$$\tan \theta_c = 2/a_0. \tag{3}$$

To that end, we point out that a_0 depends on the pulse energy and pulse duration. Thus, by varying these parameters, we can compare the θ_c measured for varying a_0 inferred from low-power measurements to Eq. (3). In the next section, we demonstrate the effectiveness of the image plate technique as a simple yet powerful diagnostic to measure the ring-like BiAD of ejected electrons and to find θ_c.

III. EXPERIMENTAL METHODS

Our experiment was performed on the VEGA-3 petawatt laser [41] at the Centro de Láseres Pulsados (CLPU) in Spain, with $\lambda_0 = 0.8\,\mu$m. A cartoon of the setup is shown in Fig. 1(a). We generated free electrons via the ionization of low-density gases ($\sim 10^{-5}$–10^{-4} mbar) to create sufficiently large electron signals that could be detected by our instrumentation. As the electrons of interest are accelerated to relativistic energies by the laser, gaining a final energy that is far greater than their energy at birth, we consider them to be at rest initially. The gas pressures were chosen low enough to reduce space charge and collective plasma effects, allowing us to work in the single-particle regime. A conservative estimate of the Debye shielding length [42,43] λ_D, for example, shows that even completely ionizing all 14 electrons of the nitrogen molecule at 10^{-4} mbar ($\sim 2.4 \times 10^{18}$ molecules/m^3), $\lambda_D \approx 0.3$ mm for 50-keV electrons and ≈ 0.4 mm for 100-keV electrons. This is much larger than the size of the focal spot, and thus allows us to ignore potential collective effects.

A. Image plates

We used two types of commercially available image plates—Fujifilm BAS-MS and BAS-SR—to image the BiAD of ejected electrons under different experimental conditions specified in Table I; images are shown in Fig. 2. Image plates store a fraction of the energy of traversing electrons

in a photostimulable phosphor layer that can be read with a phosphorimager device [44–46]. Plates with a hole (radius $\approx$10 mm) to allow the laser to pass through were mounted $\sim 40 \pm 2$ mm after the focus, perpendicular to $\vec{k}$, and facing the focal spot as shown in Fig. 1(a) (not to scale). They were covered with a single layer of Al foil (thickness 12 μm) to block scattered laser light. In the case of Figs. 2(a) and 2(b), we placed an additional Al shield (thickness 520 μm) directly in front of the plates to block the abundant low-energy electrons to enhance the contrast for the most energetic electrons of interest. This increases the detection threshold to $\sim$0.5 MeV [47] and sets the large-angle falloff to $\sim$55° according to Eq. (1), which is in good agreement with the observed large-angle falloff for the measurements as shown. After correcting for the signal fading in time [48] before the plate is read, all measurements are shown in photostimulated luminescence
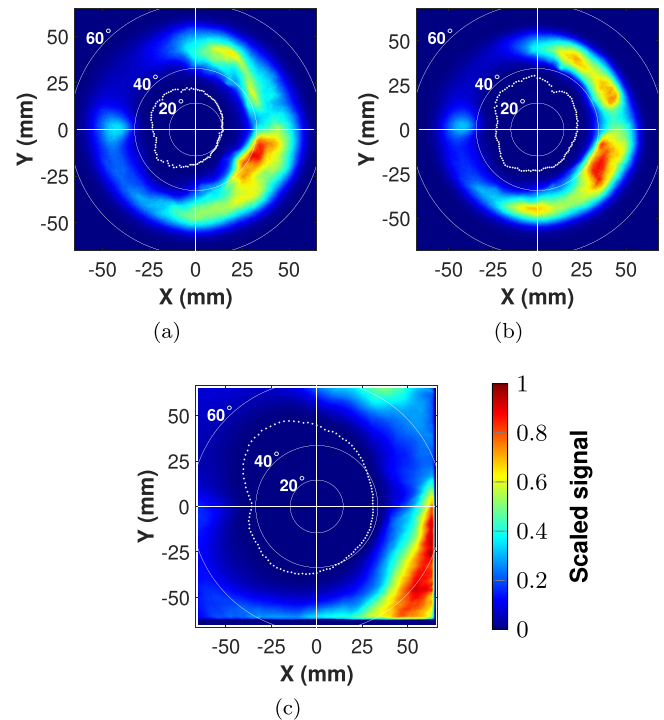

FIG. 2. Scaled image plate data captured under conditions detailed in Table I, where 1 on the color bar corresponds to peak PSL values (see text) of 7.06, 6.82, and 31.88, respectively, for (a)–(c). The laser is polarized along the $\bar{x}$ axis and $\vec{k}$ points into the page. White dots indicate the single-electron PSL level vs ϕ (see text).
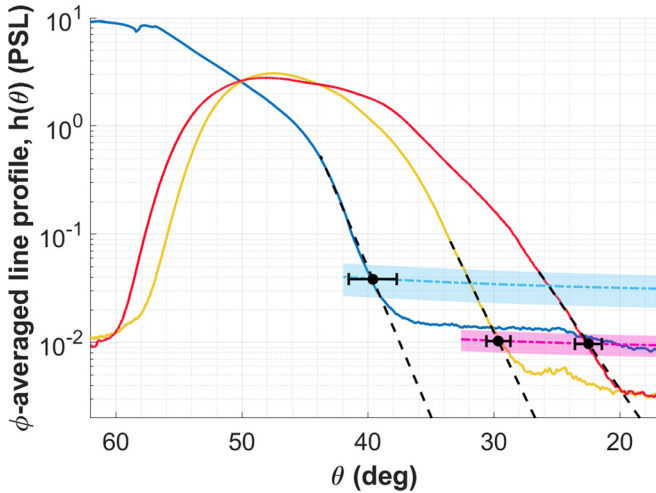
FIG. 3. The ϕ-averaged line profile, $h(\theta)$ (see text), for data in Figs. 2(a)–2(c), represented by red (far right), yellow, and dark blue (far left) curves, respectively. The dashed lines indicate exponential fits used to determine θ_c. The dot-dashed magenta (blue) curve indicates the single-electron PSL level for the BAS-SR (BAS-MS) plates used for Figs. 2(a) and 2(b) [Fig. 2(c)] and the shaded regions are the estimated uncertainties in these levels based on measurements in Ref. [50]. The solid data points represent our best estimate of θ_c and the associated uncertainty (see text).

TABLE II. Summary of experimental conditions used for measurements with the scintillation electron detectors. The U and τ (as defined in Sec. III B) reported here is the average value obtained over the corresponding sequence of shots, after considering the systematic uncertainties in the measurement process, which dominate the uncertainty in measuring the average. The techniques used to measure U and τ are detailed in Sec. III B.

Gas	U (J) ($\pm 10\%$)	τ (fs) ($\pm 20\%$)	Pressure (mbar)
N$_2$	10.6	35.6	5×10^{-5}
	26.9	40.4	3×10^{-5}
Ar	10.2	30.3	9×10^{-5}
	26.7	38.7	9×10^{-5}
Xe	10.0	31.5	4×10^{-5}
	26.4	49.7	4×10^{-5}

(PSL) units [49], which is linearly proportional to the energy deposited on the plate.

The primary goal of the analysis is to determine θ_c. This can be achieved by obtaining an average line profile for varying θ that is representative of each image, to then find the smallest θ at which the signal falls to the PSL level that a single electron would deposit. First, to remove extraneous noise from the recorded image, a median filter was applied in units of 3×3 squares of $50\,\mu$m $\times$ $50\,\mu$m pixels. The data was then visually centered using the large-angle falloff in Figs. 2(a) and 2(b) with the crosshairs shown in white, which is accurate to ± 1 mm. As the BiAD in Fig. 2(c) extends beyond the image plate, the center in this case was chosen in the vicinity of that in Figs. 2(a) and 2(b) relative to the hole cut in the plate, since the same alignment procedure was used for all three measurements. The uncertainty was extended to ± 5 mm for the measurement in Fig. 2(c). We define $g(\theta, \phi)$ as the PSL value stored in each pixel of the image, located at a given θ [$= \arctan(\sqrt{x^2 + y^2}/d)$] and ϕ [$= \arctan(y/x)$] from the laser focus [as shown in Fig. 1(a)]. A ϕ-averaged line profile, given by $h(\theta) = \int_0^{2\pi} g(\theta, \phi)d\phi / \int_0^{2\pi} d\phi$, for each image in Fig. 2 is shown in Fig. 3. We then obtain a θ_c that is representative of the recorded image by finding the smallest θ where $h(\theta) =$ the PSL value that a single electron in the MeV energy range would deposit on average in a single pixel on the image plate. This is estimated to be $\sim (9 \pm 2) \times 10^{-3}$ PSL for BAS-SR and $\sim (3 \pm 1) \times 10^{-2}$ PSL for BAS-MS from Ref. [50] for normal incidence. To account for the incident angle dependence of the deposited PSL, this value was then multiplied by $1/\cos(\theta)$ to obtain a signal floor as shown in Fig. 3. The shaded region in magenta (pale blue) represents the signal floor for the BAS-SR (BAS-MS). The point of intersection of $h(\theta)$ and the corresponding floor was used as a first estimate to then apply an

exponential fit to $h(\theta)$ from this point to an added $4°$ (toward the left in Fig. 3). We then found θ_c by extending the fit data to smaller θ to find where it crosses the shaded region, as shown in Fig. 3. To account for the uncertainty in positioning the plate, the same procedure was repeated by randomly varying the position of the center and the distance of the plate from the focus within the limits of uncertainty detailed earlier. This dominates the contribution from the uncertainty in estimating the signal floor. The final θ_c value for each measurement is reported in Table I. Additionally, to highlight the variation of the small-angle falloff position for different ϕ, the same procedure for a fixed center was applied to individual radial line profiles, $g(\theta, \phi = \phi_0)$, with $\phi_0 \in [0°, 359°]$ in steps of $3°$. These profiles were taken in strips (width 0.55 mm) to reduce fluctuations due to single-pixel noise. The position of the falloff point along each ϕ_0 is shown by the white dot markers in Fig. 2.

B. Inferring a_0

To compare the θ_c measured (Table I) to that predicted by Eq. (3), we need an estimate of a_0 for each measurement. To that end, we infer a_0 from the pulse energy U delivered on the focal plane, the temporal pulse duration τ (full width at half maximum), and images of the focal spot. Our procedure is described in detail in the Appendix of Ref. [24]. Briefly, after removing extraneous noise with a median filter in units of 3×3 pixels of the recorded image (similar to that done in Sec. III A), the pulse energy (U) is distributed over the focal spot by scaling the peak signal in the image to $I = KU/\tau$. The proportionality constant K is determined by the focal-spot distribution. Specifically, $K = C_{pk}/(C_{sum}A_{pix})$ where C_{pk} corresponds to the peak signal, C_{sum} is the total signal, and A_{pix} is the area of the camera pixel in physical units (cm^2, when I is expressed in W/cm^2).

We measured the pulse energy in the full beam through a leaky mirror before the compressor on each shot. We then factored in losses suffered from the leaky-mirror transmittivity, the compressor, the reflectivity of the tuning and parabolic mirrors, and during beam transport. We report the average U during each sequence of laser shots in Tables I and II with an overall uncertainty estimated to be $\sim \pm 10\%$ after considering the systematic uncertainties in the calibration process. We

measured τ for each laser shot by diverting a small portion of the beam from the target chamber into a second-harmonic autocorrelator placed outside a fused silica viewport (thickness 5 mm). The reported τ in Tables I and II is the average value over each sequence of laser shots after correcting for the dispersion through the viewport and $\sim$1 m of air in beam transport to the autocorrelator. We estimate that the overall uncertainty in the reported τ is $\pm$20%. The uncertainty in the precision of measuring the averages ($<$2%) is dominated by the systematic uncertainties in measuring U and τ. A representative set of focal spot images taken over different days at low power, shown in Figs. 1(b)–1(d), indicate that there is some shot-to-shot fluctuation of the focal spot distribution as well as some consistent distortions. The fluctuation in the focal spot distribution affects the peak intensity for fixed U and τ since it changes the area over which the pulse energy is distributed. Consequently, the peak intensity will decrease if there is an increase in the energy distributed away from the center of the focus. If $U = 23$ J, $\tau = 35$ fs, the peak intensity ($\propto U/\tau$) for Figs. 1(b)–1(d) would be $\sim$2.0 $\times$ 10^{20}, 1.9 $\times$ 10^{20}, and 1.5 $\times$ 10^{20} W/cm^2, respectively, assuming that these images are representative of the focus at full power. Using this method, we observed that for fixed U and τ, the fluctuation in the focal spot distribution over different laser shots across different days contributes to an uncertainty $\sim$8% in the intensity estimate. As a result, the overall uncertainty in the intensity derived from the focal spot method is estimated to be $\sim$24%. Therefore, we infer $a_0 \pm \delta a_0$ for the measurements in Figs. 2(a)–2(c) to be $\sim$9.1 $\pm$ 1.1, 7.3 $\pm$ 0.9, and 5.7 $\pm$ 0.7, respectively.

C. Scintillation electron detectors

While studying the average distribution over multiple shots reveals the average features of the laser focus, it is also important to characterize the shot-to-shot variation. We demonstrate proof of principle with the use of a scintillation electron detector that offers fast measurement capabilities, which may be extended to capture the BiAD of ejected electrons on each shot. Here, we observe shot-to-shot fluctuations for varying θ at a fixed distance from the focus in the x-z plane. We give the experimental conditions for these measurements in Table II. The detector was comprised of a bismuth germanate (BGO) scintillator crystal (thickness 3 mm), placed in front of a multipixel photon counter (MPPC) [51] that was connected to an oscilloscope to record the electron signal. The front surface of the scintillator was located at 138 mm from the laser focus. A tungsten disk (thickness 3 mm) with a 3-mm hole was used as an aperture to limit the acceptance angle to $\sim$0.37 msr. Two layers of Al foil (thickness 12 μm each), were used to block scattered laser light and the copious number of electrons with kinetic energy $\lesssim$70 keV. A layer of aluminized mylar (thickness 2 μm, with 100-nm Al on each side) was used to cover the front of the detector for added light tightness. The detector was placed on a rotary stage as shown in Fig. 1(a).

The scintillation signal recorded by the MPPC, and then registered electronically on the oscilloscope, was integrated in time for each laser shot. This signal integral per shot was then plotted as a function of angular position of the detector as shown in Fig. 4, which shows measurements made with
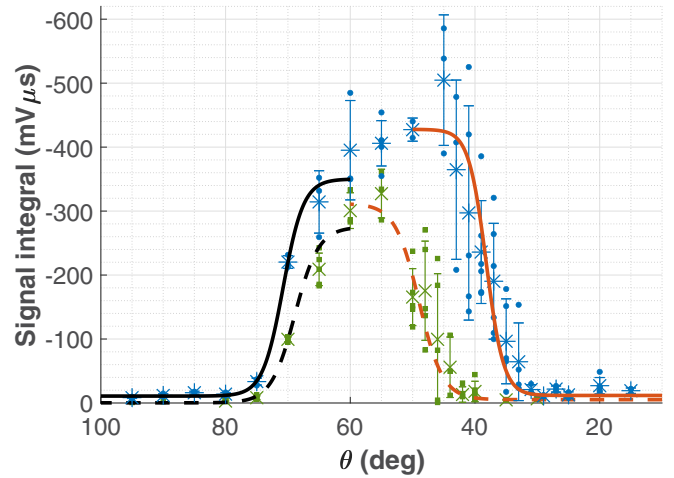

FIG. 4. Single-shot scintillation data captured with Ar gas for $15° \leqslant \theta \leqslant 95°$ with 26.7 J (blue dots) and 10.2 J (green squares) of laser energy on target for the experimental conditions detailed in Table II. The average high (low) energy data are displayed as "$*$" ("$\times$") along with their corresponding standard deviations. The solid (dashed) orange and black lines are sigmoid fits to the small and large angle falloff, respectively, for the high- (low-)energy measurement. The large angle threshold is set by the aluminum filters used to block the plethora of low-energy electrons.

Ar at low (10.2 J) and high (26.7 J) laser energy. By fitting a sigmoid $\theta > 60°$ (shown in black), we show that the large-angle falloff is independent of the laser intensity and is caused by the Al foil that blocks electrons with energy $\lesssim$70 keV [47]. This is evident from Fig. 4, where the black solid and dashed lines fall to 5% at almost the same θ ($\sim$75°). This large-angle falloff at $\theta \approx 75°$ is also consistent with the predicted energy from Eq. (1), as similarly discussed for the large-angle falloff of the image plate measurements in Sec. III A. To highlight the shift in the small-angle falloff, a sigmoid curve was fit in the range $\theta < 60°$ and $\theta < 50°$ for the low- and high-energy cases, respectively. A summary of all the sigmoid fits for the small-angle falloff can be seen in Fig. 5, which is consistent with the results from Sec. III A in that the electrons are ejected at smaller angles for higher peak intensities.

IV. DISCUSSION

From the results presented in Fig. 3, it is clear that θ_c scales with the laser energy and pulse duration, and presumably intensity. We now compare this scaling with that predicted by Eq. (3) using the a_0 estimates from Sec. III B. Figure 6 compares the measured and theoretical scaling of $\tan \theta_c$ with a_0 for the three image plate measurements in Figs. 2(a)–2(c) with $a_0 \pm \delta a_0 \approx 9.1 \pm 1.1$, 7.3 ± 0.9, and 5.7 ± 0.7, respectively. We first point out that the data is statistically consistent with $\tan \theta_c \propto 1/a_0$. It is also evident that the data is not consistent with the coefficient of 2. Fitting the experimental data to the function $\tan \theta_c = 2\eta/a_x$, to the measured data at $a_x = a_0$ (shown by the blue dashed line), $a_x = a_0 + \delta a_0$ and $a_x = a_0 - \delta a_0$ (represented by the boundaries of the shaded region), η was found to be $2.02^{+0.26}_{-0.22}$.
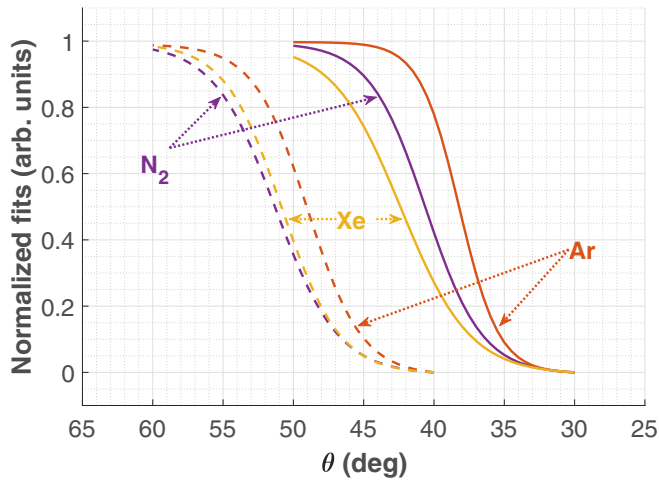
FIG. 5. Normalized and background subtracted sigmoid fits for the small-angle falloff of measurements performed with N_2 (violet), Ar (orange), and Xe (yellow). The solid (dashed) curves correspond to high (low) energy measurements.

There could be several reasons why η differs from 1: (i) the inferred a_0 might not correspond to the peak intensity present in the focus, (ii) the measured θ_c may not reflect the peak intensity in the focus, or (iii) a more robust theoretical model of the dynamics in a focused laser pulse is needed.

Here, we discuss some factors that could likely contribute to (i). First, the focal spot may not behave the same way at high power as it did at low power, and might possibly expand in size or have a larger proportion of energy distributed farther
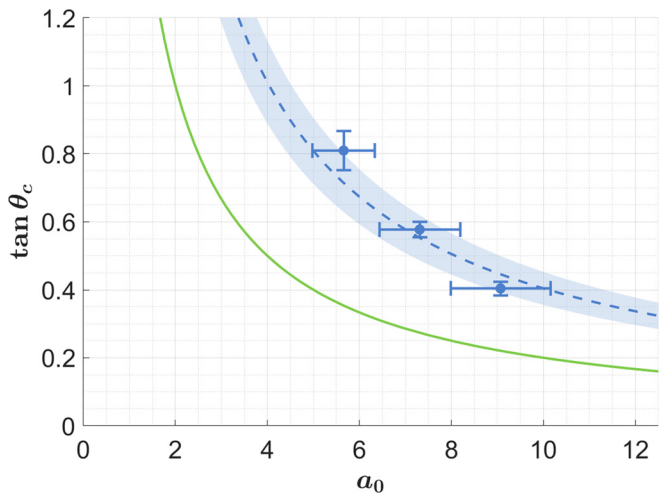

FIG. 6. Energy scaling, $\tan \theta_c$ vs inferred a_0–9.1 ± 1.1, 7.3 ± 0.9 and 5.7 ± 0.7 for the three measurements in Fig. 2 shown by blue filled circles, with Eq. (3) shown by the green solid curve. The inferred a_0 is based on the conditions given in Table I (see Sec. III B). The horizontal error bars, $\pm \delta a_0$, represent the uncertainty in calculating a_0 using the low-power focal spot image (Figs. 1(b)–1(d)). The vertical error bars represent the uncertainty in the measurement of $\tan \theta_c$ (see Sec. III A). The blue dashed line represents a numerical fit of the data to $\tan \theta_c = 2\eta/a_0$, where $\eta = 2.02^{+0.26}_{-0.22}$; the uncertainty in η is represented by the shaded region around the dashed curve.

away from the central spot. For example, it is straightforward to show that for a Gaussian beam, since $a_0 \propto 1/w_0$, the beam waist at full power would only have to expand to twice of that at low power to reduce the full power estimate of a_0 by half, which would then be a closer fit to the plane-wave model. Second, if there were a pulse front tilt, the effective pulse duration would be longer. For example, Fig. 2 of Ref. [20] shows that a tilt of only 0.2 fs/mm for a beam of 25-cm diameter (as in the VEGA-3 laser) results in a reduction of the intensity by a factor of ∼3.2. Additionally, other aberrations such as astigmatism or coma that might cause the focal spot to be oval-like or teardrop-like [such as in the central region of Figs. 1(b)–1(d)], could also contribute to lowering the intensity delivered in the focus.

To address the possibility of (ii), we note that we measured θ_c by finding the smallest θ at which the ϕ-averaged pixel response over ∼100 laser shots meets the PSL level that a single electron would deposit on average in a pixel from Ref. [50]. This intersection was found to be well above the noise (see Fig. 3), implying that the image plate was irradiated by more than one electron on average (for all ϕ) for $\theta > \theta_c$. However, if one were to perform the measurement with more laser shots, it is possible that the ϕ-averaged pixel response could reach the single-electron PSL level at a $\theta < \theta_c$. Therefore, the measured θ_c here may be used as a reasonable upper bound for the smallest ejection angle of electrons that presumably reflects the peak intensity.

A detailed simulation and additional experiments are required to address (iii), which is an ongoing project.

Another important aspect of the image plate measurements in Fig. 2 is the asymmetry in the ring-like distribution of ejected electrons around $\vec{k}$, in that there is a higher concentration of electrons on one side of each image. This asymmetry could be explained by the existence of a pulse front tilt causing a preferential sweeping of the electrons in one direction by the part that arrives earlier, creating a relative paucity of electrons on the other side. Ponderomotive ejection of electrons to one side has been reported for beams with larger phase-front tilts [52]. Further, the noticeable similarities in the distortions among the images in Fig. 2, coupled with the fact that each image is a result of ∼100 shots on different days, suggest that these distortions may be related to some consistent distortions in the beam focus. Consequently, it is plausible that detailed information about the distortions in the laser focus at full power is now accessible by measuring the BiAD of ejected electrons. We expect that studying the factors that influence the distortions in the BiAD of ejected electrons may enable a way to identify and correct for the distortions in the focus at full power. This is being investigated further with simulations modeling the interaction of the electrons with laser beams having different aberrations, as well as planned experiments.

While this manuscript explores the scaling of $\tan \theta_c$ with a_0 inferred from measurements made at low power, it may be possible to enable the direct measurement of the peak intensity by measuring θ_c. This requires gaining a better understanding of the relationship between γ_p and a_0, possibly by studying the change in γ_p for different conditions at these intensities through future experiments to test the applicability of Eq. (3).

Using θ_c alone to measure a_0 does have the limitation posed by the asymptotic behavior of $\tan \theta_c \propto 1/a_0$ that causes the relative uncertainty in a_0, $\Delta a_0 / a_0 \approx 2 \delta \theta_c / \sin 2\theta_c$, to increase rapidly as $\theta_c \to 0°$. For example, if one wishes to measure a_0 (I) to within $\pm 12.5\%$ ($\pm 25\%$) with a fixed precision in measuring θ_c, $\delta \theta_c = \pm 1°$, we can show that this method may only be usable for $\theta_c \gtrsim 8°$. In other words, with the assumption of a parametrized plane-wave model, $\tan \theta = 2\eta / a_0$, this method starts to be less effective beyond $I \approx 4\eta^2 \times 10^{20}$ W/cm^2 as the relative uncertainty $\Delta I / I$ increases rapidly. If $\eta = 2$, as measured in this experiment, this restricts the applicability of this technique to $I \lesssim 10^{21}$ W/cm^2.

Therefore, it will be important to measure γ_p over all ϕ outside this intensity range. It is critical to test Eq. (1) for smaller f/# by comparing θ_c with the ejection angle of electrons with $\gamma = \gamma_p$, to explore the limitations of applying the paraxial model to study the interaction. For these tighter focusing geometries, the substantial spread in the direction of $\vec{k}$ before and after focus may play a significant role in the scattering angle of the most energetic electrons. One may also study the onset of collective effects at higher gas pressures to estimate the range in which the electrons may be treated as single particles. Further investigations are underway to understand these effects in greater detail and to test the applicability of this approach for such cases.

V. CONCLUSION

Through this study, we have provided a technique to assess the peak intensity of petawatt-class lasers at full power by measuring θ_c and highlighted the need to study Eqs. (1) and (2) in greater detail. We have shown that the use of image plates can be an exceedingly straightforward, yet powerful, method to measure θ_c under different experimental conditions and to capture distortions in the BiAD of ejected electrons. Using the image plate measurements, we compared our experimental data to the plane-wave parametrization in Eq. (3) to find that our data, although in agreement with $\tan \theta_c \propto 1/a_0$, closely fits $\tan \theta = 2\eta / a_0$, differing from Eq. (3) by

$\eta = 2.02^{+0.26}_{-0.22}$. We discussed possible factors that could contribute to a lower peak intensity in the laser focus compared to the estimate from low-power measurements, which would then be in better agreement with the theory. We also discussed the sensitivity of the BiAD of ejected electrons to the realistic nonidealities of a high-intensity laser focus that can cause significant deviation from ideal Gaussian behavior. We have demonstrated the use of a scintillation electron detector to observe shot-to-shot fluctuations, as seen in Fig. 4, and note that it may also be extended to measure θ_c with higher sampling. A modification of this principle may also enable the measurement of the BiAD of ejected electrons over all ϕ on each shot, allowing real-time monitoring of the peak intensity, and possibly beam distortions, in the focal spot at full power. While we demonstrated the use of our instrumentation for intensities in the range of 10^{19}–10^{20} W/cm^2, we believe that these techniques could be applied to the broader range of intensities from $\sim 10^{18}$ to 10^{21} W/cm^2. This method may also hold promise at higher intensities when the acceleration of protons is expected to become relativistic in a single cycle. The techniques presented herein should aid users of high-powered laser facilities across the world and across disciplines in assessing the focal volume of petawatt-class lasers while studying numerous phenomena that occur in this intensity regime.

[1] C. Danson, D. Hillier, N. Hopps, and D. Neely, Petawatt class lasers worldwide, High Power Laser Sci. Eng. **3**, e3 (2015).

[2] J. W. Yoon, Y. G. Kim, I. W. Choi, J. H. Sung, H. W. Lee, S. K. Lee, and C. H. Nam, Realization of laser intensity over 10^{23} W/cm^2, Optica **8**, 630 (2021).

[3] J. W. Yoon, J. H. Sung, S. K. Lee, H. W. Lee, and C. H. Nam, Ultra-high intensity lasers as tools for novel physics, J. Korean Phys. Soc. **81**, 562 (2022).

[4] A. D. Piazza, L. Willingale, and J. D. Zuegel, Multi-Petawatt physics prioritization (MP3) workshop report, arXiv:2211.13187

[5] A. R. Bell and J. G. Kirk, Possibility of prolific pair production with high-power lasers, Phys. Rev. Lett. **101**, 200403 (2008).

[6] K. Krajewska, C. Müller, and J. Z. Kamiński, Bethe-Heitler pair production in ultrastrong short laser pulses, Phys. Rev. A **87**, 062107 (2013).

[7] X.-L. Zhu, T.-P. Yu, Z.-M. Sheng, Y. Yin, I. C. Edmond Turcu, and A. Pukhov, Dense GeV electron–positron pairs generated by lasers in near-critical-density plasmas, Nat. Commun. **7**, 13686 (2016).

[8] F. C. Salgado, K. Grafenstein, A. Golub, A. Döpp, A. Eckey, D. Hollatz, C. Müller, A. Seidel, D. Seipt, S. Karsch, and M. Zepf, Towards pair production in the non-perturbative regime, New J. Phys. **23**, 105002 (2021).

[9] R. Karplus and M. Neuman, Non-linear interactions between electromagnetic fields, Phys. Rev. **80**, 380 (1950).

[10] V. Costantini, B. De Tollis, and G. Pistoni, Nonlinear effects in quantum electrodynamics, Nuov. Cim. A **2**, 733 (1971).

[11] H. Gies, F. Karbstein, C. Kohlfürst, and N. Seegert, Photon-photon scattering at the high-intensity frontier, Phys. Rev. D **97**, 076002 (2018).

[12] L. Roso, R. Lera, S. Ravichandran, A. Longman, C. Z. He, J. A. Pérez-Hernández, J. I. Apiñaniz, L. D. Smith, R. Fedosejevs, and W. T. Hill III, Towards a direct measurement of the quantum-vacuum Lagrangian coupling coefficients using two counterpropagating super-intense laser pulses, New J. Phys. **24**, 025010 (2022).

[13] ZEUS, https://zeus.engin.umich.edu//.

[14] CLF Vulcan 2020 Upgrade, https://www.clf.stfc.ac.uk/Pages/Vulcan-2020.aspx.

[15] J. Bromage, S.-W. Bahk, I. A. Begishev, C. Dorrer, M. J. Guardalben, B. N. Hoffman, J. B. Oliver, R. G. Roides, E. M. Schiesser, M. J. Shoup III, M. Spilatro, B. Webb, D. Weiner, and J. D. Zuegel, Technology development for ultraintense all-OPCPA systems, High Power Laser Sci. Eng. **7**, e4 (2019).

[16] Apollon Facility, https://apollonlaserfacility.cnrs.fr/en/facility/.

[17] C. Radier, O. Chalus, M. Charbonneau, S. Thambirajah, G. Deschamps, S. David, J. Barbe, E. Etter, G. Matras, S. Ricaud, V. Leroux, C. Richard, F. Lureau, A. Baleanu, R. Banici, A. Gradinariu, C. Caldararu, C. Capiteanu, A. Naziru, B. Diaconescu *et al.*, 10 PW peak power femtosecond laser pulses at ELI-NP, High Power Laser Sci. Eng. **10**, e21 (2022).

[18] P. Yujie, X. Yi, and Y. Lianghong, Overview and status of Station of Extreme Light toward 100 PW, Reza Kenkyu **49**, 93 (2021).

[19] S. Akturk, X. Gu, P. Bowlan, and R. Trebino, Spatio-temporal couplings in ultrashort laser pulses, J. Opt. **12**, 093001 (2010).

[20] I. Ouatu, B. T. Spiers, R. Aboushelbaya, Q. Feng, M. W. von der Leyen, R. W. Paddock, R. Timmis, C. Ticos, K. M. Krushelnick, and P. A. Norreys, Ionization states for the multipetawatt laser-QED regime, Phys. Rev. E **106**, 015205 (2022).

[21] C. N. Harvey, In situ characterization of ultraintense laser pulses, Phys. Rev. Accel. Beams **21**, 114001 (2018).

[22] J. Gao, Laser intensity measurement by Thomson scattering, Appl. Phys. Lett. **88**, 091105 (2006).

[23] O. Har-Shemesh and A. Di Piazza, Peak intensity measurement of relativistic lasers via nonlinear Thomson scattering, Opt. Lett. **37**, 1352 (2012).

[24] C. Z. He, A. Longman, J. A. Pérez-Hernández, M. de Marco, C. Salgado, G. Zeraouli, G. Gatti, L. Roso, R. Fedosejevs, and W. T. Hill, Towards an in situ, full-power gauge of the focal-volume intensity of petawatt-class lasers, Opt. Express **27**, 30020 (2019).

[25] A. Link, E. A. Chowdhury, J. T. Morrison, V. M. Ovchinnikov, D. Offermann, L. Van Woerkom, R. R. Freeman, J. Pasley, E. Shipton, F. Beg, P. Rambo, J. Schwarz, M. Geissel, A. Edens, and J. L. Porter, Development of an in situ peak intensity measurement method for ultraintense single shot laser-plasma experiments at the Sandia Z petawatt facility, Rev. Sci. Instrum. **77**, 10E723 (2006).

[26] M. F. Ciappina, S. V. Popruzhenko, S. V. Bulanov, T. Ditmire, G. Korn, and S. Weber, Progress toward atomic diagnostics of ultrahigh laser intensities, Phys. Rev. A **99**, 043405 (2019).

[27] A. L. Galkin, M. P. Kalashnikov, V. K. Klinkov, V. V. Korobkin, M. Yu. Romanovsky, and O. B. Shiryaev, Electrodynamics of electron in a superintense laser field: New principles of diag-

nostics of relativistic laser intensity, Phys. Plasmas **17**, 053105 (2010).

[28] M. Kalashnikov, A. Andreev, K. Ivanov, A. Galkin, V. Korobkin, M. Romanovsky, O. Shiryaev, M. Schnuerer, J. Braenzel, and V. Trofimov, Diagnostics of peak laser intensity based on the measurement of energy of electrons emitted from laser focal region, Laser Part. Beams **33**, 361 (2015).

[29] K. A. Ivanov, I. N. Tsymbalov, O. E. Vais, S. G. Bochkarev, R. V. Volkov, V. Yu Bychenkov, and A. B. Savel'ev, Accelerated electrons for in situ peak intensity monitoring of tightly focused femtosecond laser radiation at high intensities, Plasma Phys. Controlled Fusion **60**, 105011 (2018).

[30] F. Mackenroth, A. R. Holkundkar, and H.-P. Schlenvoigt, Ultra-intense laser pulse characterization using ponderomotive electron scattering, New J. Phys. **21**, 123028 (2019).

[31] F. V. Hartemann, S. N. Fochs, G. P. Le Sage, N. C. Luhmann, J. G. Woodworth, M. D. Perry, Y. J. Chen, and A. K. Kerman, Nonlinear ponderomotive scattering of relativistic electrons by an intense laser field at focus, Phys. Rev. E **51**, 4833 (1995).

[32] B. Quesnel and P. Mora, Theory, and simulation of the interaction of ultraintense laser pulses with electrons in vacuum, Phys. Rev. E **58**, 3719 (1998).

[33] C. I. Moore, J. P. Knauer, and D. D. Meyerhofer, Observation of the transition from thomson to compton scattering in multiphoton interactions with low-energy electrons, Phys. Rev. Lett. **74**, 2439 (1995).

[34] Y. I. Salamin and F. H. M. Faisal, Ponderomotive scattering of electrons in intense laser fields, Phys. Rev. A **55**, 3678 (1997).

[35] W. L. Erikson and S. Singh, Polarization properties of Maxwell-Gaussian laser beams, Phys. Rev. E **49**, 5778 (1994).

[36] J. Pang, Y. K. Ho, X. Q. Yuan, N. Cao, Q. Kong, P. X. Wang, L. Shao, E. H. Esarey, and A. M. Sessler, Subluminous phase velocity of a focused laser beam and vacuum laser acceleration, Phys. Rev. E **66**, 066501 (2002).

[37] A. Longman and R. Fedosejevs, Modeling of high intensity orbital angular momentum beams for laser–plasma interactions, Phys. Plasmas **29**, 063109 (2022).

[38] S. C. Wilks, W. L. Kruer, M. Tabak, and A. B. Langdon, Absorption of ultra-intense laser pulses, Phys. Rev. Lett. **69**, 1383 (1992).

[39] H.-b. Cai, W. Yu, S.-p. Zhu, and C.-y. Zheng, Short-pulse laser absorption via $J \times B$ heating in ultrahigh intensity laser plasma interaction, Phys. Plasmas **13**, 113105 (2006).

[40] Y.-Q. Cui, W.-M. Wang, Z.-M. Sheng, Y.-T. Li, and J. Zhang, Laser absorption and hot electron temperature scalings in laser–plasma interactions, Plasma Phys. Controlled Fusion **55**, 085008 (2013).

[41] CLPU - Technical Features, https://www.clpu.es/en/facilties-vega-features.

[42] F. F. Chen, *Introduction to Plasma Physics, and Controlled Fusion* (Springer US, Boston, 1984).

[43] P. Bellan, *Fundamentals of Plasma Physics* (Cambridge University Press, Cambridge, 2006).

[44] K. Takahashi, K. Kohda, J. Miyahara, Y. Kanemitsu, K. Amitani, and S. Shionoya, Mechanism of photostimulated luminescence in BaFX:Eu^{2+} (X=Cl,Br) phosphors, J. Luminescence **31-32**, 266 (1984).

[45] K. Takahashi, J. Miyahara, and Y. Shibahara, Photostimulated luminescence (PSL) and color centers in BaFX:Eu2 + (X = Cl, Br, I) Phosphors, J. Electrochem. Soc. **132**, 1492 (1985).

[46] J. Miyahara, K. Takahashi, Y. Amemiya, N. Kamiya, and Y. Satow, A new type of X-ray area detector utilizing laser stimulated luminescence, Nucl. Instrum. Methods Phys. Res., Sect. A **246**, 572 (1986).

[47] Stopping Power and Range Tables for Electrons, https://physics.nist.gov/cgi-bin/Star/e_table.pl.

[48] G. Boutoux, N. Rabhi, D. Batani, A. Binet, J.-E. Ducret, K. Jakubowska, J.-P. Nègre, C. Reverdin, and I. Thfoin, Study of imaging plate detector sensitivity to 5-18 MeV electrons, Rev. Sci. Instrum. **86**, 113304 (2015).

[49] G. J. Williams, B. R. Maddox, H. Chen, S. Kojima, and M. Millecchia, Calibration, and equivalency analysis

of image plate scanners, Rev. Sci. Instrum. **85**, 11E604 (2014).

[50] T. Bonnet, M. Comet, D. Denis-Petit, F. Gobet, F. Hannachi, M. Tarisien, M. Versteegen, and M. M. Aléonard, Response functions of imaging plates to photons, electrons, and 4He particles, Rev. Sci. Instrum. **84**, 103510 (2013).

[51] MPPCs (SiPMs)/MPPC arrays|Hamamatsu Photonics, https://www.hamamatsu.com/us/en/product/optical-sensors/mppc/mppc_mppc-array.html.

[52] A. M. Wilhelm and C. G. Durfee, Tilted snowplow ponderomotive electron acceleration with spatio-temporally shaped ultrafast laser pulses, Front. Phys. **7**, 66 (2019).